A Simulation Study on the Quantitative Assessment of Tissue Microstructure With Photoacoustics

Ratan K. Saha

***Abstract*—A detailed derivation of a quantity, defined as the acoustic power per unit solid angle far from the illuminated volume divided by the intensity of the incident light beam and termed as differential photoacoustic (PA) cross section, is presented. The expression for the differential PA cross section per unit absorbing volume retains two terms, namely, the coherent and the incoherent parts. The second part based on a correlation model can be employed to analyze the PA signal power spectrum for tissue characterization. The performances of the fluid sphere, Gaussian, and exponential correlation models in assessing the mean size and the variance in the optical absorption coefficients of absorbers were investigated by performing *in silico* experiments. It was possible to evaluate diameters of solid spherical absorbers with radii $\geq$ 20 μm with an accuracy of 10% for an analysis bandwidth of 5 to 50 MHz using the first two correlation models. The accuracy of estimation was about 22% for fluid spheres mimicking erythrocytes for the third correlation model for an analysis bandwidth of 5 to 100 MHz. The extracted values of average variance in the optical absorption coefficients demonstrated good correlation with the nominal values. This study suggests that the method presented here may be developed as a potential tissue characterization tool.**

I. Introduction

A vast body of biomedical ultrasound literature deals with ultrasonic tissue characterization [1]–[5]. It aims to develop a highly sensitive method to detect and quantify small changes in tissue structure by utilizing information contained in the ultrasonic backscatter signals [3]. It has been shown that tissue structural properties such as the average scatterer size and the average acoustic concentration (i.e., the product of scatterer number density and the square of relative impedance mismatch between scatterers and the surrounding medium) can be assessed by analyzing the radio frequency (RF) echo signal power spectrum [5]. This is accomplished by fitting the measured power spectrum with a suitable theoretical scattering model based on a correlation function. A calibration spectrum is also required to normalize the power spectrum of the test material to remove system effects as well as for unbiased estimation of scatterer properties. The fluid sphere, spherical shell, Gaussian, and exponential correlation functions have been used in this context. This method has been exploited to characterize sparse biological media such as eye and prostate [6], [7]. Quantitative ultrasound images have also been generated by mapping estimates of physical properties of tissue microstructures [8]. Yu and Cloutier employed a similar method to determine mean size of red blood cell (RBC) aggregates [9]. Vlad *et al.* monitored cell death induced by radiotherapy/anticancer drugs by measuring changes in the ultrasonic spectral parameters [10]. Cancerous lesions have also been characterized using quantitative ultrasound [11], [12].

Researchers believe that similar analysis can be performed on photoacoustic (PA) signals and thus quantitative information on tissue microstructure can be extracted. Obviously, in this case, properties of light-absorbing objects distributed within the region of interest (ROI) are expected to be evaluated. Such information may become invaluable from the perspective of clinical diagnosis. Some efforts have already been made in this direction. For example, Kumon *et al.* conducted an *in vivo* study with a prostate cancer murine model and reported that PA spectral parameters have the ability to differentiate cancerous tumors from normal tissue [13]. The dependence of PA spectral features on the size of microspheres have also been examined in detail [14], [15]. Wang *et al.* demonstrated that dimensions of microparticles (radius $\approx$ 50–200 μm) hidden in turbid medium can be measured accurately with this technique [16]. It may be noted that PA technique has evolved as a potential biomedical imaging modality over the past two decades. Excellent images of small animal organs have been generated by exploiting this effect [17]–[19]. Contrast of a PA image is generally very high because PA signals are only produced by light-absorbing sites and nonabsorbing tissue components do not present any background. Desired resolution can be achieved either by choosing appropriate ultrasonic transducer or by manipulating the laser beam diameter. It can provide images at greater depths compared with conventional optical modalities because scattering of sound is two to three orders of magnitude less than that of light. In essence, it combines the most compelling features of optics and ultrasonics.

Recently, a theoretical model has been developed to study PAs from an ensemble of cells [20]. It assumes that light absorption takes place in the molecular level but acoustic emission takes place in the cellular level. It is based on the single particle approach. Essentially, PA field for a cell, approximated as a fluid sphere immersed

Manuscript received January 19, 2015; accepted February 23, 2015. The author thanks the Council of Scientific and Industrial Research (CSIR), New Delhi, India, for financial assistance.

The author is with the Surface Physics and Material Science Division, Saha Institute of Nuclear Physics, Kolkata-700 064, India (e-mail: ratank.saha@saha.ac.in).

DOI http://dx.doi.org/10.1109/TUFFC.2015.006993

in another nonabsorbing fluid, is obtained by applying a frequency domain method [21]. PA field for many cells is derived by summing those tiny fields emitted by the individual cells. The single particle approach has been successfully used to interpret experimental data in ultrasonic and light scattering problems [1], [22]. The model developed for PAs has been widely explored in the framework of forward problem formulation. For example, effects of RBC aggregation and oxygenation on PA emission have been examined [20], [23]–[25]. PAs of malaria-infected RBCs and cancer cells with endocytosed gold nanaoparticles have also been investigated exploiting this model [26], [27]. Moreover, spectral and statistical properties of PA signals from mixtures of melanoma cells (MCs) and RBCs have been probed employing this model [28]. This model in general provides intuitively expected results, which are consistent with experimental findings. These studies clearly demonstrate that PA signal power spectrum exhibits dependence on tissue microstructure. However, these studies have not been designed to solve inverse problems. In other words, average physical properties of tissue microstructures (i.e., the average size and the average variance in the optical absorption coefficients of absorbers) have not been extracted in these works by analyzing a simulated PA power spectrum.

The objective of the paper is to present an inverse problem framework to yield quantitative information on tissue microstructure. It is developed by drawing an analogy with ultrasonic scattering problems. The notion of differential PA cross section, defined as the acoustic power per unit solid angle far away from the absorbers divided by the intensity of the optical beam, is introduced, and accordingly, its analytical expression is deduced. Further, it is shown that the differential PA cross section per unit volume for a collection of absorbers can be decomposed into two components, namely, the coherent and the incoherent parts. The first component is associated with the boundary signal, whereas the second component belongs to the central segment of the signal originating from that assembly of absorbers. The analytical forms for the second part are derived for some correlation functions. Each theoretical spectrum is used to fit the measured PA signal power spectrum for evaluating tissue parameters. The performance of the fluid sphere, Gaussian, and exponential correlation functions are examined in this work using simulated PA signals. Such signals were generated from various types of tissue-mimicking samples consisting of monodisperse, bidisperse, and polydisperse suspensions of spherical absorbers. A Monte Carlo algorithm was implemented to construct 3-D tissue realizations. It is found that the dimensions of solid light-absorbing particles with radii $\geq$20 μm can be assessed with good accuracy (<10%). The average size of fluid spheres imitating RBCs is estimated with an accuracy of about 22%. The variance in the optical absorption coefficients of absorbers estimates demonstrates good correlation with the nominal values.

The organization of the paper is as follows. The inverse problem framework is derived in detail in Section II. Section III describes the simulation methodology including the spectral analysis procedure. Simulation results are illustrated in Section IV. Finally, discussion and conclusions from this study are presented in Section V.

II. Inverse Problem Framework

A. Differential PA Cross Section

The time dependent wave equation for the pressure field generated due to absorption of light by a region can be obtained using the linearized equations of fluid dynamics and is given by [16]:

$$\frac{\partial^2}{\partial t^2}\, p(\mathbf{r},t) - c^2\nabla^2 p(\mathbf{r},t) = \Gamma\mu(\mathbf{r})\frac{\partial h_{\mathrm{L}}(t)}{\partial t}, \tag{1}$$

where Γ, μ, and c are the Grüneisen parameter, light absorption coefficient, and speed of sound for the absorbing region, respectively; h_{L} is the temporal envelope of the laser beam. It is assumed in deriving (1) that no heat conduction takes place before the acoustic pulse is launched. The time-independent wave equation can readily be derived by substituting the Fourier transforms $p(\mathbf{r},t) = \int \tilde{p}(\mathbf{r},f)e^{-i2\pi ft}\,\mathrm{d}\,f$ and $\partial h_{\mathrm{L}}(t)/\partial t = \int(-i2\pi f)H_{\mathrm{L}}(f)e^{-i2\pi ft}\,\mathrm{d}\,f$ into (1) and that yields [16],

$$\nabla^2\tilde{p}(\mathbf{r},f) + k^2\tilde{p}(\mathbf{r},f) = \frac{ik\Gamma\mu(\mathbf{r})}{c}\,H_{\mathrm{L}}(f), \tag{2}$$

where f is the frequency and $k = 2\pi f/c$ is the wavenumber. The term on the right side of (2) is referred to as the source term, which arises due to an optical inhomogeneity. The acoustic properties of this region are similar to that of the surrounding medium. The solution to (2) in the far field for a uniformly illuminated light-absorbing fluid region suspended in a nonabsorbing fluid medium can be written as [16],

$$\tilde{p}(\mathbf{r},f) = \frac{ik\Gamma H_{\mathrm{L}}(f)}{c}\int_V \mu(\mathbf{r}')\frac{e^{ik|\mathbf{r}-\mathbf{r}'|}}{4\pi|\mathbf{r}-\mathbf{r}'|}\,\mathrm{d}^3\,\mathbf{r}' \approx M(\mathbf{k})\frac{e^{ikr}}{r}, \tag{3}$$

where $e^{ik|\mathbf{r}-\mathbf{r}'|}/(4\pi|\mathbf{r}-\mathbf{r}'|)$ is the free-space Green's function and

$$M(\mathbf{k}) = \frac{ik\Gamma H_{\mathrm{L}}(f)}{4\pi c}\int_V \mu(\mathbf{r}')e^{-i\mathbf{k}\cdot\mathbf{r}'}\,\mathrm{d}^3\,\mathbf{r}'. \tag{4}$$

The differential PA cross section (i.e., as defined earlier, the acoustic power received into a solid angle in the asymptotic region divided by the intensity of the incident optical radiation) can be expressed as

$$\sigma(k) = \frac{|M(\mathbf{k})|^2}{2\rho c H_{\mathrm{L}}(f)}, \tag{5}$$

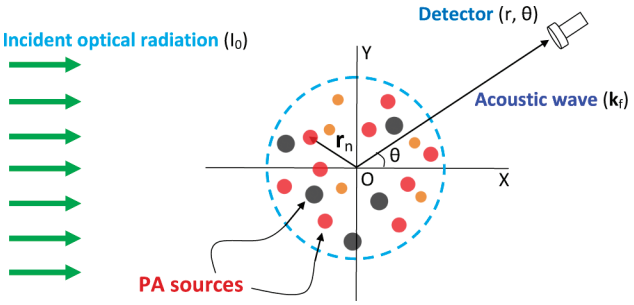

Fig. 1. Schematic diagram displaying the relevant geometry.

where ρ is the density of the surrounding medium. The total PA cross section, which represents a hypothetical area, can be computed by integrating the differential PA cross section over the whole solid angle. It can be thought by drawing an analogy with a scattering cross section that energy corresponding to this area of the incident light beam converts into acoustic energy due to the PA effect.

For a homogeneous light-absorbing sphere, the integration in (4) can be carried out analytically, yielding

$$\sigma(k) = \frac{\Gamma^2 H_{\mathrm{L}}(f)}{2\rho c^3}\mu^2 a^4 [j_1(ka)]^2, \tag{6}$$

where a is the radius of the sphere and j_1 is the spherical Bessel function of first kind of order unity. Eq. (6) states that $\sigma(k)$ is omnidirectional. In the small particle limit, i.e., $ka \to 0$, the Bessel function $j_1(ka) \to ka/3$, (6) simplifies into

$$\sigma(k) = \frac{\Gamma^2 H_{\mathrm{L}}(f)}{18\rho c^3}\mu^2 k^2 a^6. \tag{7}$$

It can be noticed from (7) that PA cross section exhibits k^2 dependence, whereas light or acoustic scattering cross section shows k^4 dependence in the Rayleigh particle limit. Moreover, the former linearly depends upon the intensity of the incident flux; however, the latter is independent of the intensity of the incident radiation.

For an optically inhomogeneous medium, the differential PA cross section per unit absorbing volume can be written as

$$\begin{aligned}\chi(k) &= \frac{\langle\!|M(\mathbf{k})|^2\rangle}{2\rho c H_{\mathrm{L}}(f)V},\\ &= \frac{k^2\Gamma^2 H_{\mathrm{L}}(f)}{32\pi^2 c^3 \rho V}\left\langle \int_V \mu(\mathbf{r}_1')e^{-i\mathbf{k}\cdot\mathbf{r}_1'}\,\mathrm{d}^3\,\mathbf{r}_1' \int_V \mu(\mathbf{r}_2')e^{i\mathbf{k}\cdot\mathbf{r}_2'}\,\mathrm{d}^3\,\mathbf{r}_2' \right\rangle,\\ &= \frac{k^2\Gamma^2 H_{\mathrm{L}}(f)}{32\pi^2 c^3 \rho V}\int_V\int_V \langle \mu(\mathbf{r}_1')\mu(\mathbf{r}_2')\rangle e^{-i\mathbf{k}\cdot(\mathbf{r}_1'-\mathbf{r}_2')}\,\mathrm{d}^3\,\mathbf{r}_1'\,\mathrm{d}^3\,\mathbf{r}_2',\end{aligned} \tag{8}$$

where V is the absorbing volume and the notation $\langle\rangle$ denotes the ensemble average (i.e., measurements need to be carried out over many different possible configurations of absorbers and the average value is determined from those measured values). The relevant geometry is shown in Fig. 1. Eq. (8) is obtained by drawing an analogy with ultrasonic scattering from tissue. Moreover, the same quantity when measured in the backward direction is referred to as the backscatter coefficient, which has been extensively used for ultrasonic tissue characterization [1]. Eq. (8), after some simple mathematical manipulations, reduces to [5],

$$\begin{aligned}\chi(k) = \frac{k^2\Gamma^2 H_{\mathrm{L}}(f)}{32\pi^2 c^3 \rho}\Big[\Big|\langle\mu\rangle\int_V e^{-i\mathbf{k}\cdot\Delta\mathbf{r}}\,\mathrm{d}^3\,\Delta\mathbf{r}\Big|^2\\ +\langle\!|\mu-\langle\mu\rangle|^2\rangle\int_{-\infty}^{\infty} b_\mu(\Delta\mathbf{r})e^{-i\mathbf{k}\cdot\Delta\mathbf{r}}\,\mathrm{d}^3\,\Delta\mathbf{r}\Big],\end{aligned} \tag{9}$$

where $\Delta\mathbf{r}$ denotes the difference of coordinates, i.e., $\Delta\mathbf{r} = \mathbf{r}_1' - \mathbf{r}_2'$. Eq. (9) has two parts. The first part is the coherent component, which arises from in phase addition of tiny signals by PA sources. It is known that coherent addition of signals takes place at boundary of a cloud of PA sources resulting in strong boundary buildup [26], [29]. On other hand, incoherent addition of signals from randomly located PA sources gives rise to the second part. The middle segment of a PA trace corresponding to the central region of the cloud represents such a signal [26], [29]. PA power from individual sources adds up independently for this part. Here, $b_\mu(\Delta\mathbf{r})$ is the correlation coefficient and can be expressed as

$$b_\mu(\Delta\mathbf{r}) = \frac{\langle\!(\mu(\mathbf{r}_1') - \langle\mu(\mathbf{r}_1')\rangle)(\mu(\mathbf{r}_2') - \langle\mu(\mathbf{r}_2')\rangle)\rangle\!\rangle}{\langle\!|\mu-\langle\mu\rangle|^2\rangle}. \tag{10}$$

It depends on the structure of the medium and varies from $b_\mu(0) = 1$ to $b_\mu(\infty) = 0$. Further, for a statistically isotropic medium, $b_\mu(\Delta\mathbf{r})$ can be replaced with $b_\mu(\Delta r)$ (i.e., the correlation coefficient only depends on the magnitude of $\Delta\mathbf{r}$ but not on its direction). Therefore, for a statistically isotropic medium, angular coordinates may be integrated over, leading to a simple form for the second part of (9):

$$\begin{aligned}\chi(k) = \frac{k^2\Gamma^2 H_{\mathrm{L}}(f)}{32\pi^2 c^3 \rho}\langle\!|\mu-\langle\mu\rangle|^2\rangle\frac{4\pi}{k}\\ \times\int_0^{\infty} b_\mu(\Delta r)\Delta r\sin(k\Delta r)\,\mathrm{d}\,\Delta r.\end{aligned} \tag{11}$$

In the present work, it has been illustrated how the structural properties of uniformly illuminated optically inhomogeneous medium can be characterized from the incoherent component of the differential PA cross section per unit volume.

B. Correlation Models

Three correlation models, namely the fluid sphere, Gaussian, and exponential functions, are considered in this study to assess tissue microstructure. These are simple mathematical functions and can provide simple closed form analytical expressions for the differential PA cross

section per unit volume for a statistically isotropic medium. These functions were originally suggested in the context of scattering of electromagnetic and acoustic waves in the ocean and atmosphere [30]. These have also been successfully utilized to evaluate structural parameters of tissue using ultrasound scatter data [4], [5], [31], [32]. In the first model, the irradiated volume is assumed to contain fluidlike absorbing spheres with radius ϱ_1, and these particles are suspended in a nonabsorbing fluid medium. The three dimensional correlation coefficient for a fluid sphere is [1], [5], [33],

$$b_\mu(\Delta r) = \begin{cases} 1 - \dfrac{3\Delta r}{4\varrho_1} + \dfrac{\Delta r^3}{16\varrho_1^3}, & \Delta r \le 2\varrho_1, \\ 0, & \Delta r > 2\varrho_1. \end{cases} \tag{12}$$

The differential PA cross section per unit absorbing volume in this model can easily be calculated by substituting (12) into (11) and is equal to

$$\begin{aligned} \chi_1(k) &= \frac{k^2\Gamma^2 H_{\mathrm{L}}(f)}{32\pi^2 c^3 \rho} \langle\!| \mu - \langle\mu\rangle|^2 \rangle \frac{4\pi}{k} \\ &\quad \times \int_0^{2\varrho_1} \left[1 - \frac{3\Delta r}{4\varrho_1} + \frac{\Delta r^3}{16\varrho_1^3}\right] \Delta r \sin(k\Delta r)\, \mathrm{d}\,\Delta r, \\ &= \frac{k^2\Gamma^2 H_{\mathrm{L}}(f)}{32\pi^2 c^3 \rho} \bar{\mu}_{\mathrm{var}} \frac{4\pi}{k} \frac{3\varrho_1}{k} [j_1(k\varrho_1)]^2, \\ &= \frac{k^2\Gamma^2 H_{\mathrm{L}}(f)}{32\pi^2 c^3 \rho} \bar{\mu}_{\mathrm{var}} V_{\mathrm{abs}} \left[\frac{3}{k\varrho_1} j_1(k\varrho_1)\right]^2, \end{aligned} \tag{13}$$

where $V_{\mathrm{abs}} = \int_{-\infty}^{\infty} b_\mu(\Delta r)\, \mathrm{d}\,\Delta r = (4/3)\pi\varrho_1^3$ is the volume of the fluid particle; $\bar{\mu}_{\mathrm{var}} = \langle|\mu - \langle\mu\rangle|^2\rangle$. For a small PA source or in the long wavelength limit [i.e., $k\varrho_1 \to 0$ and then $j_1(k\varrho_1) \to k\varrho_1/3$], (13) becomes

$$\chi_0 = \frac{k^2\Gamma^2 H_{\mathrm{L}}(f)}{32\pi^2 c^3 \rho} \bar{\mu}_{\mathrm{var}} V_{\mathrm{abs}}. \tag{14}$$

From (13) and (14), we can define PA intensity form factor as the ratio of differential PA cross section per unit volume for a test material with finite absorber size to the same quantity for a similar light-absorbing region containing point absorbers and is given by

$$\hat{F}_1(k) = \chi_1/\chi_0 = \left[\frac{3}{k\varrho_1} j_1(k\varrho_1)\right]^2. \quad \text{(Fluid sphere)} \tag{15}$$

The form factor depicts how χ_1 depends on the geometry of the absorber. The variation of $\hat{F}_1$ with $k\varrho$ is displayed in Fig. 2. It shows that $\hat{F}_1 \approx 1$ when $k\varrho \ll 1$ and for $k\varrho \le 1$, $\hat{F}_1$ is a decreasing function [5]. However, $\hat{F}_1$ exhibits complicated variation for $k\varrho \ge 1$ [5]. It may be noted that acoustic scattering intensity form factor, an analog of (15), can be found in literature and that has been used in many studies to characterize tissue microstructure [5], [8].

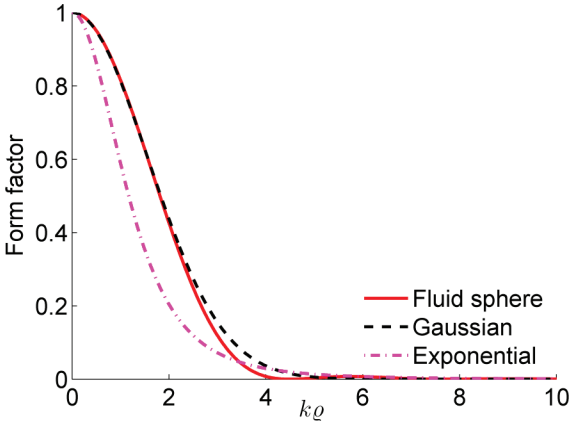

Fig. 2. Plots of form factors for various correlation functions.

In the second model, PA sources are assumed to be random continua (i.e., continuously varying fluctuations in the optical absorption coefficients), which can be described by

$$b_\mu(\Delta r) = e^{-[(\Delta r^2)/(2\varrho_2^2)]}, \tag{16}$$

where characteristic dimension ϱ_2 represents the radius of PA source. The expression for differential PA cross section per unit volume for the Gaussian correlation model can be derived by substituting (16) into (11), yielding

$$\begin{aligned} \chi_2(k) &= \frac{k^2\Gamma^2 H_{\mathrm{L}}(f)}{32\pi^2 c^3 \rho} \langle\!| \mu - \langle\mu\rangle|^2 \rangle \frac{4\pi}{k} \\ &\quad \times \int_0^{\infty} \exp\left(-\frac{\Delta r^2}{2\varrho_2^2}\right) \Delta r \sin(k\Delta r)\, \mathrm{d}\,\Delta r, \\ &= \frac{k^2\Gamma^2 H_{\mathrm{L}}(f)}{32\pi^2 c^3 \rho} \bar{\mu}_{\mathrm{var}} \frac{4\pi}{k} \sqrt{\frac{\pi}{2}} k\varrho_2^3 \exp\left(-\frac{k^2\varrho_2^2}{2}\right), \\ &= \frac{k^2\Gamma^2 H_{\mathrm{L}}(f)}{32\pi^2 c^3 \rho} \bar{\mu}_{\mathrm{var}} V_{\mathrm{abs}} \exp\left(-\frac{k^2\varrho_2^2}{2}\right), \end{aligned} \tag{17}$$

where $V_{\mathrm{abs}} = \int_{-\infty}^{\infty} b_\mu(\Delta r)\, \mathrm{d}\,\Delta r = (2\pi\varrho_2^2)^{(3/2)}$. Further, it can be shown by equating (17) and (13) in the small particle limit that $\varrho_2 = (2/(9\pi))^{1/6}\varrho_1$. The PA form factor for this correlation model can be recognized as

$$\hat{F}_2(k) = \exp\left(-\frac{k^2\varrho_2^2}{2}\right). \quad \text{(Gaussian)} \tag{18}$$

The variation of $\hat{F}_2$ with $k\varrho$ is illustrated in Fig. 2.

In the third model, the illuminated medium is hypothesized to be composed of randomly distributed continuously varying fluctuations in the optical absorption coefficients, which may be mimicked by an exponential function, such as

$$b_\mu(\Delta r) = e^{-(\Delta r/\varrho_3)}, \tag{19}$$

where ϱ_3 denotes the characteristic dimension of PA source. The corresponding formula for differential PA

cross section per unit volume for the exponential correlation model is

$$\begin{aligned}\chi_3(k) &= \frac{k^2\Gamma^2 H_{\mathrm{L}}(f)}{32\pi^2 c^3 \rho}\langle|\mu - \langle\mu\rangle|^2\rangle \frac{4\pi}{k} \\ &\quad \times \int_0^\infty \exp\left(-\frac{\Delta r}{\varrho_3}\right)\Delta r \sin(k\Delta r)\,\mathrm{d}\,\Delta r, \\ &= \frac{k^2\Gamma^2 H_{\mathrm{L}}(f)}{32\pi^2 c^3 \rho}\,\overline{\mu}_{\mathrm{var}}\,\frac{4\pi}{k}\,\frac{2k\varrho_3^3}{(1+k^2\varrho_3^2)^2}, \\ &= \frac{k^2\Gamma^2 H_{\mathrm{L}}(f)}{32\pi^2 c^3 \rho}\,\overline{\mu}_{\mathrm{var}} V_{\mathrm{abs}}\,\frac{1}{(1+k^2\varrho_3^2)^2}.\end{aligned} \tag{20}$$

where $V_{\mathrm{abs}} = \int_{-\infty}^{\infty} b_\mu(\Delta r)\,\mathrm{d}\,\Delta r = 8\pi\varrho_3^3$. It is related to ϱ_1 as $\varrho_3 = (1/6)^{1/3}\,\varrho_1$. The simple expression for the form factor may be found as

$$\hat{F}_3(k) = \frac{1}{(1+k^2\varrho_3^2)^2}. \quad \text{(Exponential)} \tag{21}$$

The plot of $\hat{F}_3$ with $k\varrho$ is demonstrated in Fig. 2. Note that the derivative of the Gaussian function is zero at $\Delta r = 0$. However, the derivative of the exponential function differs from zero at $\Delta r = 0$; this is possible if the absorption coefficient is a discontinuous function at $\Delta r = 0$. This may not represent a physical situation, and therefore, a modified version was suggested to overcome this limitation [30].

III. Materials and Methods

A. Numerical Phantoms

The performance of correlation models presented above have been assessed by conducting *in silico* experiments. For this purpose, various types of phantoms were constructed. In case of the first type of samples, spherical monodisperse polystyrene beads were randomly positioned under nonoverlapping conditions within the irradiated volume using a Monte Carlo method known as random sequential adsorption (RSA) technique [34]. The size of ROI was taken as $4000 \times 750 \times 750$ $\mu\mathrm{m}^3$, which was occupied by beads with identical optical absorption coefficients at a volume fraction of 0.05. This phantom was designed to mimic an experimental work [16]. The laser beam propagated along the x-direction and acoustic waves propagated along the −x-direction were collected in the far field regime using a point receiver. The backward mode was preferred because it is suitable for *in vivo* applications. The second type of samples were prepared with polydisperse spherical beads via the RSA approach. However, in this case, beads with the largest size were placed first and coordinates of smaller particles were generated sequentially thereafter [35]. The size distribution of beads followed a Gaussian distribution in each sample having a standard deviation ≈10% of the mean radius. The motivation to investigate this set of samples was to examine how size dispersity of absorbers would affect accuracy of these models in estimating tissue parameters.

The PA technique has been applied extensively to study blood because it produces strong PA signals at certain optical wavelengths owing to the presence of hemoglobin as an endogenous chromophore. For example, blood vessels have been imaged with great details using PA tomography [17]–[19]; total hemoglobin concentration and blood oxygen saturation have also been quantified with PAs [36], [37]. A natural question is how the inverse problem framework would work for characterizing blood samples. To address this question, samples containing monodisperse and polydisperse RBCs with the same μ values were investigated. The size of the irradiated volume was fixed at $4000 \times 100 \times 100$ $\mu\mathrm{m}^3$. Each cell was approximated as a fluid sphere. The same RSA technique was employed in these cases to obtain spatial locations of nonoverlapping RBCs. A series of samples with hematocrits 1, 2, 3, 4, 5, and 10% were investigated. It might be mentioned here that normal level of hematocrit in human whole blood is close to 40%. Finally, several samples consisting of mixtures of RBCs and MCs were tested. In this case, number of MCs was gradually increased but that of RBCs was decreased so that cellular volume fraction remained fixed at 0.05 for all samples. Tissue configurations were simulated using the RSA method by placing MCs followed by positioning of RBCs within the 3-D volume [28]. Such samples were probed in this work to study whether we could develop a method for detecting MCs in blood exploiting PA tissue characterization technique. Note that attempts have been made by many groups to detect MCs in circulation with PAs [38]–[40]. The detection of circulating tumor cells is extremely helpful to diagnose, stage, and treat cancer.

B. PA Signal Simulation

The detailed derivation of PA field generated by a spherical absorber can be found in literature [21], [41]. It essentially solves time-independent wave equations inside and outside the absorber in spherical polar coordinates and the expression for PA field is obtained by matching boundary conditions (namely, continuity of the pressure and the normal component of the particle velocity) on the surface of PA source. The expressions for PA fields pertaining to various situations are invoked in this study and presented below in brief.

1) PA Signal From Polystyrene Beads: Exact analytical expression for PA field generated by a solid sphere under the uniform illumination by an intensity-modulated laser beam is given in [41]. Such a solution can be extended through the use of the linear superposition principle in deriving PA field produced by an ensemble of spheres in the

$$\tilde{p}(\mathbf{r},f) \approx \frac{iK_{\mathrm{b}}\beta_{\mathrm{b}}\mu_{\mathrm{b}}I_0}{\rho_{\mathrm{b}}C_{\mathrm{Pb}}v_{\mathrm{lb}}r}\sum_{n=1}^{N_{\mathrm{b}}}a_{\mathrm{b}n}^2\frac{j_1(\hat{q}_{\mathrm{b}n})e^{ik_{\mathrm{f}}(r-a_{\mathrm{b}n})}}{\left(1-\hat{\rho}+\hat{\rho}\frac{\tilde{v}^2}{\hat{q}_{\mathrm{b}n}^2}\right)\frac{\sin\hat{q}_{\mathrm{b}n}}{\hat{q}_{\mathrm{b}n}}-\left(1+\hat{\rho}\frac{\tilde{v}^2}{\hat{q}_{\mathrm{b}n}^2}\right)\cos\hat{q}_{\mathrm{b}n}+i\hat{\rho}\hat{v}\left[\left(1-\frac{\tilde{v}^2}{\hat{q}_{\mathrm{b}n}^2}\right)\sin\hat{q}_{\mathrm{b}n}+\frac{\tilde{v}^2}{\hat{q}_{\mathrm{b}n}}\cos\hat{q}_{\mathrm{b}n}\right]}e^{-i\mathbf{k}_{\mathrm{f}}\cdot\mathbf{r}_{\mathrm{b}n}},$$
$$\hat{q}_{\mathrm{b}n}=2\pi f a_{\mathbf{b}n}/v_{\mathrm{lb}},\quad k_{\mathrm{f}}=2\pi f/v_{\mathrm{f}},\quad \hat{\rho}=\rho_{\mathrm{b}}/\rho_{\mathrm{f}},\quad \hat{v}=v_{\mathrm{lb}}/v_{\mathrm{f}},\quad \tilde{v}=2v_{\mathrm{tb}}/v_{\mathrm{lb}}, \tag{22}$$

$$p(\mathbf{r},t)\approx\frac{iK_{\mathrm{b}}\beta_{\mathrm{b}}\mu_{\mathrm{b}}F}{2\pi\rho_{\mathrm{b}}C_{\mathrm{Pb}}v_{\mathrm{lb}}r}\int_{\infty}^{\infty}\mathrm{d}\,\omega\left[\sum_{n=1}^{N_{\mathrm{b}}}a_{\mathrm{b}n}^2\frac{j_1(\hat{q}_{\mathrm{b}n})e^{i(k_{\mathrm{f}}r-k_{\mathrm{f}}\boldsymbol{a}_{\mathrm{b}n}-\omega t)}}{\left(1-\hat{\rho}+\hat{\rho}\frac{\tilde{v}^2}{\hat{q}_{bn}^2}\right)\frac{\sin\hat{q}_{\mathrm{b}n}}{\hat{q}_{bn}}-\left(1+\hat{\rho}\frac{\tilde{v}^2}{\hat{q}_{\mathrm{b}n}^2}\right)\cos\hat{q}_{\mathrm{b}n}+i\hat{\rho}\hat{v}\left[\left(1-\frac{\tilde{v}^2}{\hat{q}_{\mathrm{b}n}^2}\right)\sin\hat{q}_{\mathrm{b}n}+\frac{\tilde{v}^2}{\hat{q}_{bn}}\cos\hat{q}_{\mathrm{b}n}\right]}e^{-i\mathbf{k}_{\mathrm{f}}\cdot\mathbf{r}_{\mathrm{b}n}}\right], \tag{23}$$

asymptotic region as in (22), see above, where subscripts b and f indicate polystyrene bead and ambient fluid medium, respectively; $a_{\mathrm{b}n}$ is the radius of the nth sphere; K_{b}, β_{b}, C_{Pb}, and μ_{b} are the bulk modulus, thermal expansion coefficient, heat capacity, and light absorption coefficient for the solid medium, respectively; I_0 is the intensity of the laser beam; and N_{b} is the total number of beads present within ROI. Here, ρ_{b}, v_{lb}, and v_{tb} denote the density, longitudinal, and transverse sound speeds for the solid medium, respectively; and ρ_{f} and v_{f} represent the density and speed of sound for the surrounding medium, respectively. Further, $\mathbf{k}_{\mathrm{f}}$ defines the direction of measurement. The time domain PA response for a delta function deposition of heat can easily be determined using the Fourier transform as in (23), see above, where F is the optical fluence. Eq. (23) was evaluated numerically to obtain complex pressure data for a collection of polystyrene beads. The real part of that provided the PA signal.

2) PA Signal From RBCs: Similarly, the expression of a PA field emitted by a fluid sphere, when uniformly irradiated by an optical radiation, is available in the literature [21]. The PA field emitted by a collection of RBCs approximated as fluid spheres can be cast in terms of the single particle solution as [20],

$$\tilde{p}(\mathbf{r},f)\approx\frac{i\beta_{\mathrm{e}}\mu_{\mathrm{e}}I_0v_{\mathrm{e}}}{C_{\mathrm{Pe}}r}\times\sum_{n=1}^{N_{\mathrm{e}}}a_{\mathrm{e}n}^2\frac{j_1(\hat{q}_{en})e^{ik_{\mathrm{f}}(r-a_{\mathrm{e}n})}}{(1-\hat{\rho})\frac{\sin\hat{q}_{en}}{\hat{q}_{en}}-\cos\hat{q}_{en}+i\hat{\rho}\hat{v}\sin\hat{q}_{en}}e^{-i\mathbf{k}_{\mathrm{f}}\cdot\mathbf{r}_{en}},$$
$$\hat{q}_{en}=2\pi f a_{en}/v_{\mathrm{e}},\quad \hat{\rho}=\rho_{\mathrm{e}}/\rho_{\mathrm{f}},\quad \hat{v}=v_{\mathrm{e}}/v_{\mathrm{f}}, \tag{24}$$

where subscript e indicates erythrocyte and $\mathbf{r}_{en}$ is the position vector of the nth RBC. Here, a_{en}, ρ_{e}, and v_{e} correspond to radius of the nth RBC, density, and speed of sound for RBC, respectively. Associated time-dependent pressure for a delta function heating pulse becomes

$$p(\mathbf{r},t)\approx\frac{i\beta_{\mathrm{e}}\mu_{\mathrm{e}}Fv_{\mathrm{e}}}{2\pi C_{\mathrm{Pe}}r}\int_{\infty}^{\infty}d\omega\times\left[\sum_{n=1}^{N_{\mathrm{e}}}a_{en}^2\frac{j_1(\hat{q}_{en})e^{i(k_{\mathrm{f}}r-k_{\mathrm{f}}a_{en}-\omega t)}}{(1-\hat{\rho})\frac{\sin\hat{q}_{en}}{\hat{q}_{en}}-\cos\hat{q}_{en}+i\hat{\rho}\hat{v}\sin\hat{q}_{en}}e^{-i\mathbf{k}_{\mathrm{f}}\cdot\mathbf{r}_{en}}\right]. \tag{25}$$

Time series of PA pressure for many RBCs were acquired in this work by performing numerical integration.

3) PA Signal From a Mixture of RBCs and MCs: The PA field generated by a mixture of RBCs and MCs can be expressed as [28],

$$\tilde{p}(\mathbf{r},f)\approx\left[\frac{i\beta_{\mathrm{e}}\mu_{\mathrm{e}}I_0v_{\mathrm{e}}a_{\mathrm{e}}^2}{C_{\mathrm{Pe}}}\phi_e\sum_{n=1}^{N_{\mathrm{e}}}e^{-i\mathbf{k}_{\mathrm{f}}\cdot\mathbf{r}_{en}}+\frac{i\beta_{\mathrm{m}}\mu_{\mathrm{m}}I_0v_{\mathrm{m}}\boldsymbol{a}_{\mathrm{m}}^2}{C_{\mathrm{Pm}}}\phi_{\mathrm{m}}\sum_{s=1}^{N_{\mathrm{m}}}e^{-i\mathbf{k}_{\mathrm{f}}\cdot\mathbf{r}_{\mathrm{m}s}}\right]\frac{e^{ik_{\mathrm{f}}r}}{r}, \tag{26}$$

where

$$\phi_{\mathrm{e}}=\frac{j_1(\hat{q}_{\mathrm{e}})e^{-ik_{\mathrm{f}}a_{\mathrm{e}}}}{\left[(1-\hat{\rho}_{\mathrm{e}})\frac{\sin(\hat{q}_{\mathrm{e}})}{\hat{q}_{\mathrm{e}}}-\cos(\hat{q}_{\mathrm{e}})+i\hat{\rho}_{\mathrm{e}}\hat{v}_{\mathrm{e}}\sin(\hat{q}_{\mathbf{e}})\right]},\quad \hat{q}_{\mathrm{e}}=2\pi f a_{\mathrm{e}}/v_{\mathrm{e}},\quad \hat{\rho}_{\mathrm{e}}=\rho_{\mathrm{e}}/\rho_{\mathrm{f}},\quad \hat{v}_{\mathrm{e}}=v_{\mathrm{e}}/v_{\mathrm{f}}, \tag{27}$$

and

$$\phi_{\mathrm{m}}=\frac{j_1(\hat{q}_{\mathrm{m}})e^{-ik_{\mathrm{f}}a_{\mathrm{m}}}}{\left[(1-\hat{\rho}_{\mathrm{m}})\frac{\sin(\hat{q}_{\mathrm{m}})}{\hat{q}_{\mathrm{m}}}-\cos(\hat{q}_{\mathrm{m}})+i\hat{\rho}_{\mathrm{m}}\hat{v}_{\mathrm{m}}\sin(\hat{q}_{\mathbf{m}})\right]},\quad \hat{q}_{\mathrm{m}}=2\pi f a_{\mathrm{m}}/v_{\mathrm{m}},\quad \hat{\rho}_{\mathrm{m}}=\rho_{\mathrm{m}}/\rho_{\mathrm{f}},\quad \hat{v}_{\mathrm{m}}=v_{\mathrm{m}}/v_{\mathrm{f}}, \tag{28}$$

where subscript m is used to refer melanocyte; and $\mathbf{r}_{\mathrm{m}s}$ represents the position vector for the sth MC. Here, a_{m}, ρ_{m}, and v_{m} specify the radius, density, and speed of sound

TABLE I. PHYSICAL PROPERTIES OF POLYSTYRENE BEADS USED IN SIMULATIONS.

ρ_{f} (kg/m^3)	1005
v_{f} (m/s)	1540
ρ_{b} (kg/m^3)	1050
v_{lb} (m/s)	2350
v_{tb} (m/s)	1120
K_{b} (kg·m^{-1}s^{-2})	1.0
C_{Pb} (J·kg^{-1}·K^{-1})	1.0
β_{b} (K^{-1})	1.0
μ_{b} (m^{-1})	10.0
F (J·m^{-2})	1.0

for MC, respectively. Time-dependent pressure field for uniform illumination of cells by a delta function laser pulse can be cast as [28],

$$p(\mathbf{r},t) \approx \frac{iF}{2\pi}\int_{-\infty}^{\infty} \mathrm{d}\,\omega \left[\frac{\beta_{\mathrm{e}}\mu_{\mathrm{e}} v_{\mathrm{e}} a_{\mathrm{e}}^2}{C_{\mathrm{Pe}}}\,\phi_{\mathrm{e}} \sum_{n=1}^{N_{\mathrm{e}}} e^{-i\mathbf{k}_{\mathrm{f}}\cdot\mathbf{r}_{en}} + \frac{\beta_{\mathrm{m}}\mu_{\mathbf{m}} v_{\mathrm{m}} a_{\mathrm{m}}^2}{C_{\mathrm{Pm}}}\,\phi_{\mathrm{m}} \sum_{s=1}^{N_{\mathrm{m}}} e^{-i\mathbf{k}_{\mathrm{f}}\cdot\mathbf{r}_{ms}} \right] \frac{e^{i(k_{\mathrm{f}}r-\omega t)}}{r}, \tag{29}$$

Eq. (29) was computed in this study to obtain RF lines for mixtures of RBCs and MCs.

C. Choice of the Simulation Parameters

The PA signal from a collection of beads was obtained by calculating (23). The contributions from a wide range of frequencies (0.001 to 1000 MHz with a step of 0.125 MHz) were summed up and the pressure signal was sampled at a frequency of 2 GHz. The density, longitudinal sound speed, and transverse sound speed for the solid were considered to be $\rho_{\mathrm{b}} = 1050$ kg/m^3, $v_{\mathrm{lb}} = 2350$ m/s, and $v_{\mathrm{tb}} = 1120$ m/s, respectively [42]. The density and speed of sound for the ambient medium were taken as $\rho_{\mathrm{f}} = 1005$ kg/m^3 and $v_{\mathrm{f}} = 1540$ m/s, respectively. The parameters K_{b}, β_{b}, C_{Pb}, μ_{b}, and F scale the magnitude of PA signal, but do not modify its frequency dependence. Therefore, they were treated as constants in this study. Numerical values of simulation parameters are summarized in Table I.

The PA signals from suspensions of monodisperse and polydisperse RBCs were simulated by computing (25). On the other hand, (29) was calculated yielding PA signals from mixtures of RBCs and MCs. The density and speed of sound for RBCs were assumed to be $\rho_{\mathrm{e}} = 1092$ kg/m^3 and $v_{\mathrm{e}} = 1639$ m/s, respectively, and for MCs were taken as $\rho_{\mathrm{m}} = 1150$ kg/m^3 and $v_{\mathrm{m}} = 1639$ m/s, respectively [28]. It might be noted that cellular light absorption coefficient for RBC could be estimated to be $\mu_{\mathrm{e}} = 1771.8$ m^{-1} at 639 nm for 75% oxygen saturation [28]. It could be obtained from literature for MC as $\mu_{\mathrm{m}} = 29\,852.2$ m^{-1} at the same irradiating wavelength [28]. It could be thought that PA signals were generated at 639 nm incident radiation from diluted blood samples at 75% oxygen saturation resembling MCs suspended in diluted venous blood. This was chosen because some veins are easily accessible (such as superficial dorsal veins in the hand) and may thus be suitable for *in vivo* applications. Numerical values of various cell parameters are displayed in Table II.

TABLE II. PHYSICAL PROPERTIES OF RBCS AND MCS USED IN SIMULATIONS.

a_{e} (μm)	2.75
a_{m} (μm)	5.0
ρ_{f} (kg/m^3)	1005
v_{f} (m/s)	1540
ρ_{e} (kg/m^3)	1092
v_{e} (m/s)	1639
ρ_{m} (kg/m^3)	1150
v_{m} (m/s)	1639
C_{Pe} (J·kg^{-1}·K^{-1})	1.0
C_{Pm} (J·kg^{-1}·K^{-1})	0.87
β_{e} (K^{-1})	1.0
β_{m} (K^{-1})	1.0
μ_{e} (m^{-1})	1771.8
μ_{m} (m^{-1})	29 852.2
F (J·m^{-2})	1.0

D. Parameter Estimation

As discussed above, average variance in the optical absorption coefficients and average particle size of a test sample could be estimated by analyzing PA spectral data. However, to achieve these, measurement from a known sample was required. The spectral analysis procedure was similar to that of [16]. At first average power spectrum for a test sample was obtained by taking the Fourier transform of simulated signals, such as

$$S(k) = \frac{1}{N}\sum_{n=1}^{N} |P_n(k)|^2 \tag{30}$$

where N indicates the number of measurements. Signal segment associated with the central part of the sample was chosen because for this portion incoherent addition took place. A representative plot of PA signal is illustrated in Fig. 3(a). The simulated signal was generated by an ensemble of monodisperse polystyrene beads of radius 10 μm when they filled 5% of the total illuminated volume. To improve the clarity of the figure, the RF line is sampled at 40 MHz (however, spectral analysis was performed using raw signals sampled at 2 GHz). The sample length is denoted by the two vertical bars (solid lines). The power spectrum has been calculated using the segment enclosed by the rectangle as shown in the figure. In this portion, tiny signals from spherical sources randomly distributed in 3-D space add up in random phase varying from 0 to 2π. PA signals emitted by sources positioned within two vertical bars (solid and dashed lines, which are separated by 154 μm) in each boundary are partially correlated and contribute to boundary buildup [26], [27], [29]. As an example in this case, we consider constructive interference of 5-MHz acoustic waves only. The lengths over which sources are partially correlated are smaller for higher frequency

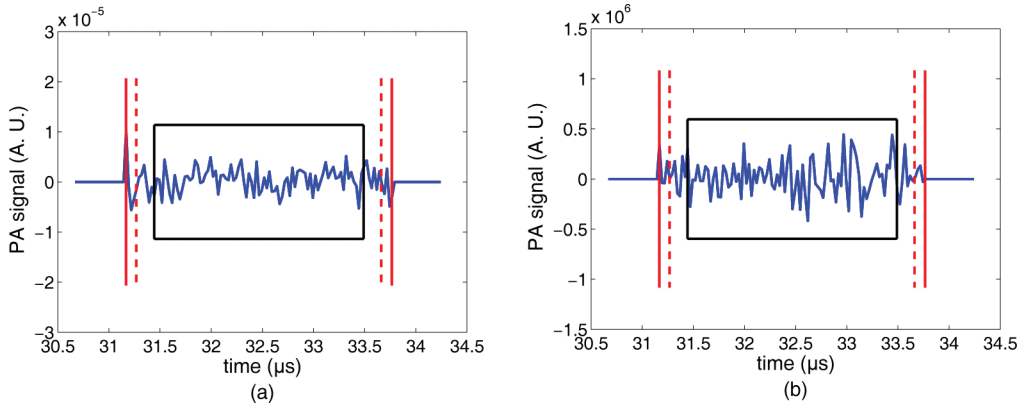

Fig. 3. (a) Plot of a simulated RF line generated by a collection of monodisperse polystyrene beads of radius 10 μm (0.05 being the volume fraction occupied by beads). RF line is sampled at 40 MHz for clarity of the figure (however, spectral analysis was performed on raw signals sampled at 2 GHz). The outermost vertical bars outline the sample length. The distance between two vertical bars (solid and dashed lines) at each boundary is about 154 μm and PA sources within this region are partially correlated with respect to the acoustic wave of frequency 5 MHz. The signal segment within the rectangular box was utilized for spectrum analysis. (b) Similar to (a) but for a sample with monodisperse RBCs at 5% hematocrit.

waves and longer for lower frequency waves. Further, amplitude of the boundary signal is comparable with that of the central region because concentration of PA sources is small in this case. However, it could become very strong at higher concentration of sources as was observed in earlier studies [26], [27], [29]. An analogous signal from RBCs at 5% hematocrit is displayed in Fig. 3(b). The volume of the central segment considered for spectral analysis is ≈3154 × 750 × 750 μm^3 for the bead samples and ≈3154 × 100 × 100 μm^3 for the blood samples.

The average power spectrum as given by (30) was obtained for the test material and also for the calibration medium. The difference spectrum thereafter calculated by dividing $S_t(k)$ with $S_c(k)$:

$$S_{\text{diff}}(k) = \frac{S_t(k)}{S_c(k)}. \tag{31}$$

where subscripts t and c denote test and calibration spectrum, respectively; the subscript diff indicates difference spectrum. The difference spectrum was further normalized by its maximum and the average absorber size of the test sample was estimated by minimizing the following equation within the desired bandwidth with respect to ϱ_t as

$$\left| \frac{\hat{F}(k,\varrho_t)}{\hat{F}(k,\varrho_c)} - \frac{S_{\text{diff}}(k)}{\max[S_{\text{diff}}(k)]} \right|^2 = \text{minimum}, \tag{32}$$

where ϱ_c is the average particle size of the reference medium. For each set of samples, the first sample acted as the reference medium. The calibration spectrum was derived from this medium. To estimate the average size of absorbers of the test medium, ϱ_t was varied between 0.2 to 30 ϱ_c at a step of 0.05, and at each step, the sum of the squares of the errors over the analysis bandwidth obtained from (32) was stored. The size corresponding to the lowest error was accepted as the estimated size. This procedure was followed for each form factor model.

Once the average size of the absorbers for the test sample was estimated, its value was utilized to estimate $\overline{\mu}_{\text{var}}$ by conducting the following minimization,

$$\left| \frac{\chi_t(k,\varrho_t)}{\chi_c(k,\varrho_c)} - \frac{S_t(k)}{S_c(k)} \right|^2 = \text{minimum}, \tag{33}$$

where χ_t and χ_c state differential PA cross section per unit volume for the test and the known samples, respectively, and the optimization was carried out within the same

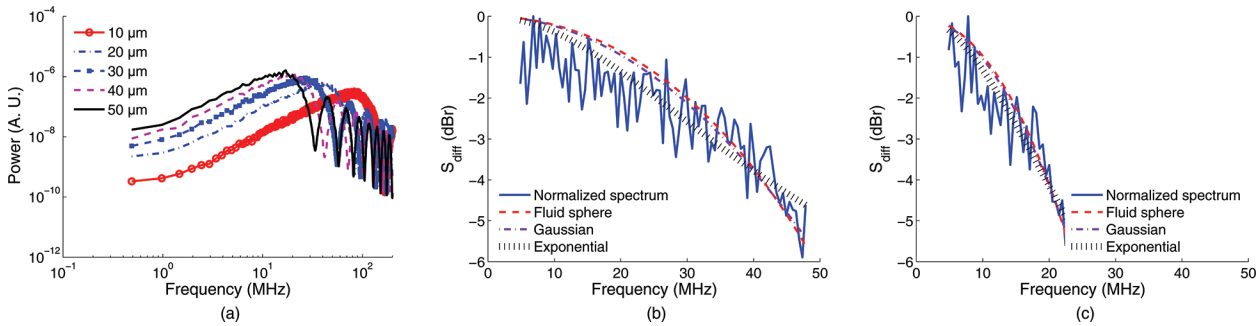

Fig. 4. (a) PA spectral lines for different samples composed of monodisperse polystyrene beads. (b) Plot of difference spectrum for a sample containing beads with size $a_b = 20$ μm. The calibration spectrum was obtained from the sample containing 10-μm beads. Broken lines represent fitted curves for the three correlation models. (c) Same as (a) but for $a_b = 40$ μm.

TABLE III. THE NOMINAL AND THE ESTIMATED VALUES OF THE MEAN SIZE AND THE VARIANCE IN THE OPTICAL ABSORPTION COEFFICIENTS FOR SUSPENSIONS OF MONODISPERSE POLYSTYRENE BEADS.

Nominal			Fluid sphere			Gaussian			Exponential		
ϱ (μm)	$\bar{\mu}_{\text{var}}$ (m^{-2})	Frequency band (MHz)	ϱ (μm)	$\bar{\mu}_{\text{var}}$ (m^{-2})	Err	ϱ (μm)	$\bar{\mu}_{\text{var}}$ (m^{-2})	Err	ϱ (μm)	$\bar{\mu}_{\text{var}}$ (m^{-2})	Err
10.0	4.75	4.9–86.9	10.0	4.75	0	10.0	4.75	0	10.0	4.75	0
20.0	4.75	4.9–47.9	20.9	4.25	8.1	21.7	4.00	8.0	17.6	7.50	7.3
30.0	4.75	4.9–28.3	30.4	4.00	2.4	31.0	4.00	2.4	22.4	10.50	2.3
40.0	4.75	4.9–23.4	40.4	4.00	1.6	41.4	3.75	1.6	29.4	10.75	1.4
50.0	4.75	4.9–18.6	47.4	4.25	0.8	48.3	4.00	0.8	33.1	12.75	0.8

The volume fraction occupied by beads is about 0.05. The sum of the relative residual norms (Err $= \Sigma_i |(o_i - e_i)|/|e_i|$, where o_i and e_i indicate observed and expected values, respectively) examining goodness of fitting of each correlation model is also presented.

bandwidth employed in the previous optimization. Essentially, $\bar{\mu}_{\text{var}}$ was known for the reference medium but was not known for a test medium. Therefore, $\bar{\mu}_{\text{var,t}}$ was gradually changed from 0.00002 to 100 $\bar{\mu}_{\text{var,c}}$ with an increment of 0.25 ($\bar{\mu}_{\text{var,t}}$ and $\bar{\mu}_{\text{var,c}}$ denote $\bar{\mu}_{\text{var}}$ of the test and the reference media, respectively), and at each increment, sum of the squares of the errors over the bandwidth of interest provided by (33) was recorded. Thereafter, $\bar{\mu}_{\text{var}}$ estimate for the test material was chosen from those $\bar{\mu}_{\text{var,t}}$ values for which error was the minimum. These steps were repeated for each correlation model.

For the first two types of samples, the lower limit of the analysis bandwidth was set to 5 MHz so that the gated signal length becomes around 10 wavelengths with respect to this frequency. It is reported in the literature that estimations become independent of gate length if it is more than 10 wavelengths of the center frequency of the transducer used [11], [43]. The frequency corresponding to the first maximum of the power spectrum curve [Fig. 3(a)], for each sample to be analyzed, was taken as the upper limit. This bandwidth was sufficient to provide good size estimates for samples containing solid particles. For the blood samples, the optimization was performed approximately between 5 to 100 MHz. This was chosen because a similar spectral region was analyzed for characterization of cell pellet biophantoms and tumors using ultrasonic backscatter signals in a recent study [44]. For each sample, an average power spectrum was obtained from 100 RF lines by performing frequency domain averaging. Those RF lines were computed from 100 different tissue realizations. The average power spectrum curve was used for spectral analysis. In addition to that, for samples with polystyrene beads, raw spectral data were used for the analysis. Nevertheless, for the other samples, spectral data were processed using the "smooth" function of Matlab (The MathWorks Inc., Natick, MA, USA) over a span of 21 points to improve accuracy of estimation.

IV. SIMULATION RESULTS

Plots of average PA spectra for different samples with monodisperse polystyrene beads are demonstrated in Fig. 4(a). Each power spectrum curve was obtained from 100 RF lines. The well-known peak and dip pattern can be seen for each line from this figure. The first minimum appears at lower frequency for larger particles and vice versa. Note that the position of first minimum is a signature of particle size. The spectral power increases with in-

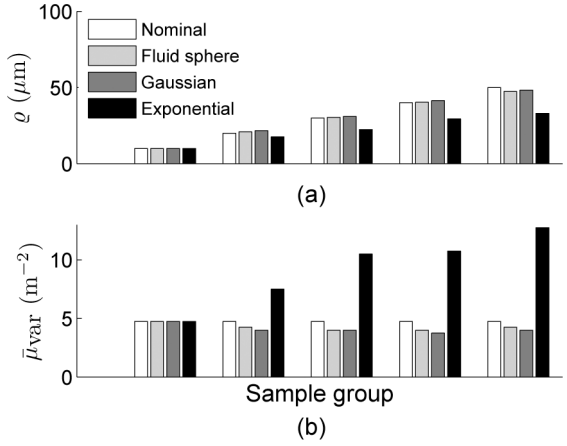

Fig. 5. (a) A comparative study between the nominal and the estimated radii for samples composed of light-absorbing monodisperse polystyrene beads suspended in agarose medium. (b) Bar diagram for extracted values of the mean variance in the optical absorption coefficients.

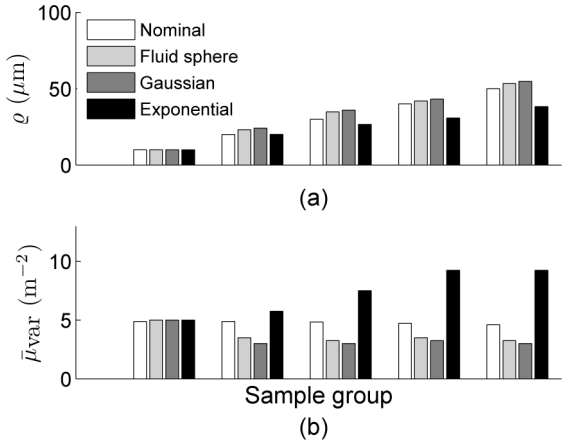

Fig. 6. Chart displaying the estimated values with respect to the veridical values for polydisperse beads: (a) for mean radius of absorbers, and (b) for mean variance in the optical absorption coefficients.

TABLE IV. THE EXTRACTED PARAMETERS FROM SAMPLES WITH POLYDISPERSE POLYSTYRENE BEADS FILLING APPROXIMATELY 5% OF THE IRRADIATED VOLUME.

Nominal		Frequency band	Fluid sphere			Gaussian			Exponential		
ϱ (μm)	$\overline{\mu}_{\text{var}}$ (m^{-2})	(MHz)	ϱ (μm)	$\overline{\mu}_{\text{var}}$ (m^{-2})	Err	ϱ (μm)	$\overline{\mu}_{\text{var}}$ (m^{-2})	Err	ϱ (μm)	$\overline{\mu}_{\text{var}}$ (m^{-2})	Err
10.0 ± 1.0	4.88	4.9–86.9	10.0	5.00	0	10.0	5.00	0	10.0	5.00	0
20.0 ± 2.0	4.87	4.9–47.9	23.2	3.50	12.3	24.3	3.00	12.0	20.1	5.75	10.9
30.0 ± 2.9	4.83	4.9–28.4	34.9	3.25	3.1	36.0	3.00	3.0	26.6	7.50	2.5
40.0 ± 3.8	4.73	4.9–23.4	42.0	3.50	1.6	43.2	3.25	1.6	30.9	9.25	1.5
50.0 ± 4.5	4.60	4.9–18.6	53.3	3.25	0.9	54.8	3.00	0.9	38.2	9.25	0.9

Err $= \Sigma_i|(o_i - e_i)|/|e_i|$ defines the fitting error for a correlation model (where o_i and e_i state observed and expected values, respectively).

creasing bead size. This trend can be seen up to ≈20 MHz and after that power spectrum curves overlap. The difference spectrum (normalized by its maximum) for a sample consisting of particles with $a_{\text{b}} = 20$ μm is shown in Fig. 4(b). The same curve for another sample ($a_{\text{b}} = 40$ μm) is displayed in Fig. 4(c). The curve corresponding to $a_{\text{b}} = 10$ μm has been treated as the calibration spectrum. The fitted lines for various correlation models are also drawn in each figure. The estimated values of the mean size and the variance in the optical absorption coefficients are summarized in Table III. The frequency bandwidth considered during analysis is also given for each case. The nominal and the estimated sphere diameters agree within 5, 3, and 34% for the fluid sphere, Gaussian, and exponential models, respectively. The variances of the optical absorption coefficients for various samples are underestimated by the first two models. The estimates agree within 16 and 21% in these cases. However, the extracted values are overestimated by the third model and differ greatly with respect to the nominal values. Irrespective of the accuracy of the estimated parameters, the correlation models provide excellent fits to the simulated spectrum [Figs. 4(b) and 4(c)]. The sum of the relative residual norms assessing goodness of a fit is displayed in Table III. The correlation models produce similar errors while fitting a simulated spectrum. The evaluated parameters are also presented in Fig. 5 for better visualization. The nominal values are given in the same figure for comparison. For the exponential model, estimated mean absorber sizes are smaller but the evaluated variances in the optical absorption coefficients are higher compared with the actual values; however, the fits remain good.

Similar results for polydisperse polystyrene beads embedded in agarose medium are presented in Table IV, and the estimates are portrayed in Fig. 6. It is clear from Table IV that the first model provides marginally better size estimates than the second model. The third model becomes inferior compared with the others for particles with mean radius >20 μm. As in the previous case, $\overline{\mu}_{\text{var}}$ estimates are underestimated by the first two models but overestimated by the third model. Similar observation can also be made from Fig. 6. The fitting errors of the three models are comparable (see columns 6, 9, and 12 of Table IV). For the both monodisperse and polydisperse cases, the fluid sphere correlation model is better than the other models.

Some representative power spectrum curves for diluted blood samples are illustrated in Fig. 7(a). The lines are well separated and spectral intensity at each frequency increases as the hematocrit increases. The difference spectrum for 2% hematocrit is shown in Fig. 7(b) and that for 4% hematocrit is illustrated in Fig. 7(c). The calibration spectrum has been determined from the sample with 1% hematocrit. The difference spectrum curves are drawn over a large frequency range. Figs. 7(b) and 7(c) also display the fitted lines for the three correlation functions. In general, the correlation models do not provide good fits to the simulated power spectral lines. Numerical values for the mean size and average variance in the optical absorption coefficients are given in Tables V and VI for monodisperse and polydisperse suspensions of RBCs, respectively. Both the nominal and the estimated values are presented. The same quantities are also plotted in Figs. 8 and 9, respectively, for those samples. It is evident from Table V

TABLE V. NUMERICAL VALUES OF SEVERAL PARAMETERS OBTAINED FROM DILUTED BLOOD SAMPLES CONSISTING OF MONODIPERSE RBCS AT 1, 2, 3, 4, 5, AND 10% HEMATOCRITS.

Nominal			Fluid sphere			Gaussian			Exponential		
ϱ (μm)	$\overline{\mu}_{\text{var}}$ (10^4 m^{-2})	Frequency band (MHz)	ϱ (μm)	$\overline{\mu}_{\text{var}}$ (10^4 m^{-2})	Err	ϱ (μm)	$\overline{\mu}_{\text{var}}$ (10^4 m^{-2})	Err	ϱ (μm)	$\overline{\mu}_{\text{var}}$ (10^4 m^{-2})	Err
2.75	3.11	4.9–96.7	2.75	3.00	0	2.75	3.00	0	2.75	3.00	0
2.75	6.15	4.9–96.7	3.35	3.25	14.4	3.35	3.25	14.4	3.05	4.50	16.8
2.75	9.14	4.9–96.7	3.30	5.00	11.5	3.35	4.75	11.6	3.05	6.25	11.7
2.75	12.05	4.9–96.7	3.35	5.75	9.0	3.35	5.75	9.0	3.05	7.75	9.3
2.75	14.91	4.9–96.7	3.45	6.25	11.6	3.45	6.25	11.6	3.10	8.75	12.1
2.75	28.25	4.9–96.7	3.85	6.25	15.4	3.90	6.00	15.5	3.35	9.75	16.3

Fitting error (Err $= \Sigma_i|(o_i - e_i)|/|e_i|$, where o_i and e_i denote observed and expected values, respectively) is also displayed.

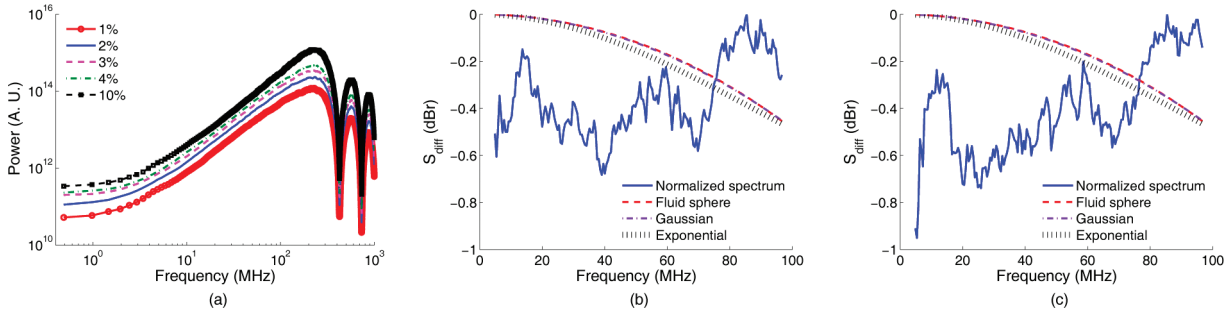

Fig. 7. (a) PA spectral lines for a series of diluted blood samples composed of monodisperse RBCs. Blood hematocrit is given in the legend. (b)-(c) Plots of difference spectra for 2 and 4% hematocrits, respectively. Fitted lines by the three correlation models are also presented in the same graphs. The power spectrum corresponding to 1% hematocrit acted as the calibration spectrum.

that for each correlation model, size estimate increases when hematocrit level is gradually raised. The first two models facilitate comparable size estimates. The exponential model works better than the former models. For instance, associated error is about 22% for the exponential model and 42% for the others. The other extracted parameter $\overline{\mu}_{\text{var}}$ exhibits a monotonic rise with increasing hematocrit. It also follows the same trend as that of the actual quantity (see column 2 of Table V). Similar variations can be seen in Table VI. The numerical values of errors examining goodness of fits are similar for all three models (see columns 6, 9, and 12 of Tables V and VI).

Fig. 10(a) displays some spectral lines computed from different mixtures of MCs and RBCs. These cells occupy a volume fraction of 0.05 in each case. For comparison, spectral line corresponding to the monodisperse sample with 5% hematocrit is also shown in the same figure. Besides, this medium has acted as a reference medium. The first minimum for the monodisperse sample appears nearly at 426 MHz and can be linked to the size of RBC [28]. For other lines, the first minimum occurs approximately at 234 MHz and can be attributed to the size of MC [28]. The spectral power at each frequency increases with increasing number of MCs. Typical difference spectra including the fitted lines by the three correlation functions are given in Figs. 10(b) and 10(c). Tissue characterization parameters are quantified in Table VII for several samples for the three correlation models and also displayed in Fig. 11 for better presentation. Table VII illustrates that average size increases slowly but $\overline{\mu}_{\text{var}}$ increases rapidly with growing number of MCs in blood. It seems that MCs play a dominant role in this case because of their strong light absorption property. It is clear from Table VII and Fig. 11 that the first two models provide similar estimates for ρ and $\overline{\mu}_{\text{var}}$. The estimated average absorber size remains almost constant and is significantly higher than the nominal value for each mixture. The other extracted parameter shows excellent agreement with the actual value for all samples (error is approximately within 6.5%). For the third model, the estimated size is smaller in comparison with that of the first two models but $\overline{\mu}_{\text{var}}$ is overestimated. These models facilitate good fits to the difference spectrum curves. The sum of the relative residual norms is small for each sample. For each case, $\overline{\mu}_{\text{var}}$ increases as the number of MCs within the irradiated volume increases and demonstrate good correlation with the nominal parameter.

V. Discussion and Conclusions

An inverse problem framework characterizing optically heterogeneous media is discussed. Various correlation functions are used to analyze incoherent PA signals. The mean size and the average variance in the optical absorption coefficients of absorbing particles are estimated. The approach described in this paper relies on the spectral matching technique to determine average particle size. This is a very reliable technique and the accuracy of this method does not depend on the experimental condition

TABLE VI. A Comparison Between the Veridical and the Estimated Values for Suspensions of Polydisperse RBCs at 1, 2, 3, 4, 5, and 10% Hematocrits.

Nominal			Fluid sphere			Gaussian			Exponential		
ϱ (μm)	$\overline{\mu}_{\text{var}}$ (10^4 m^{-2})	Frequency band (MHz)	ϱ (μm)	$\overline{\mu}_{\text{var}}$ (10^4 m^{-2})	Err	ϱ (μm)	$\overline{\mu}_{\text{var}}$ (10^4 m^{-2})	Err	ϱ (μm)	$\overline{\mu}_{\text{var}}$ (10^4 m^{-2})	Err
2.75 ± 0.27	3.19	4.9–96.7	2.75	3.25	0	2.75	3.25	0	2.75	3.25	0
2.75 ± 0.27	6.32	4.9–96.7	3.35	3.50	12.1	3.35	3.50	12.0	3.05	4.50	9.7
2.75 ± 0.27	9.39	4.9–96.7	3.25	5.25	11.4	3.25	5.25	11.4	3.00	6.75	12.0
2.75 ± 0.27	12.38	4.9–96.7	3.40	5.75	9.3	3.45	5.50	9.4	3.05	8.00	9.3
2.75 ± 0.27	15.32	4.9–96.7	3.30	7.25	8.5	3.30	7.25	8.5	3.00	9.75	8.7
2.75 ± 0.27	28.97	4.9–96.7	3.85	6.50	16.1	3.90	6.25	16.3	3.35	10.00	16.7

The accuracy of fitting is also quantified (Err = $\Sigma_i|(o_i - e_i)|/|e_i|$, where o_i and e_i denote observed and expected values, respectively).

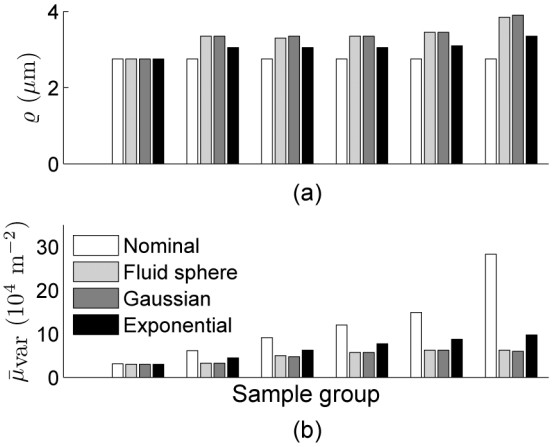

Fig. 8. Diagrams displaying assessed tissue parameters from diluted blood samples with monodisperse RBCs [mean size of absorbers in (a) and average variance in the optical absorption coefficients of PA sources in (b)].

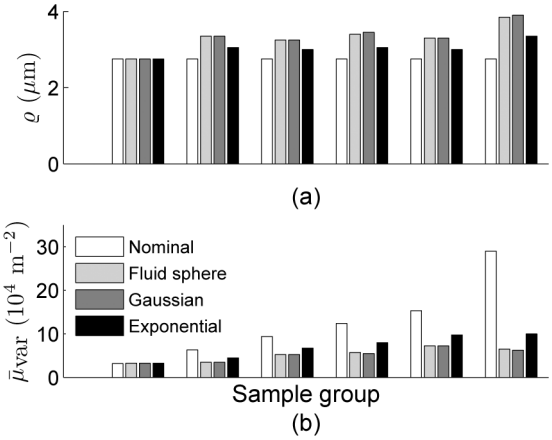

Fig. 9. (a) A comparison between the nominal and the estimated radii of absorbers for samples composed of polydisperse RBCs. (b) Similar to (a) but for the variance in the optical absorption coefficients.

(such as temperature). Nevertheless, it works at its best if the spectral slope varies significantly within the analysis bandwidth. For example, for polystyrene beads, spectral slopes change a lot within the analysis bandwidth, and hence, accurate size information is yielded [see Tables III and IV and Figs. 4(b), 4(c), 5(a), and 6(a)]. Figs. 7(b) and 7(c) demonstrate that spectral slopes almost remain flat over the analysis bandwidth because blood samples are composed of spherical absorbers of identical/similar size (identical size for monodisperse samples and similar size for polydisperse cases). Consequently, the methods presented here become less sensitive and provide relatively inferior size estimates compared with the case of beads. For the case of mixtures of RBCs and MCs, spectral slopes vary in a similar way for all samples because they contain bidisperse spheres at different proportions. As a result of that, size estimates do not differ appreciably for each model [e.g., see column 4 of Table VII and Fig. 11(a)]. Moreover, these models interpret that average particle size increases greatly as MCs are introduced in the illuminated volume. Even an addition of a small number of MCs to blood can have a significant impact on the estimated size (see row 2 in Table VII). This is in accordance with the ultrasonic literature [45]. Tuthill *et al.* [45] revealed that strong but occasional scatterers embedded in tissue greatly altered ultrasonic backscatter signal properties.

The estimates of average variance in the optical absorption coefficients for bead samples have not been assessed as accurately as the size estimates. It may be speculated that for solid particles the speed of sound and density are very different with respect to the ambient medium and they may have contributed to errors. This is also observed in quantitative ultrasound [5]. The product of scatterer number density and the square of relative impedance mismatch between scatterers and the surrounding medium could not be extracted accurately [5]. The evaluated values of $\overline{\mu}_{\mathrm{var}}$ for the diluted blood samples differ significantly in comparison with the nominal values, particularly at higher hematocrits. Nevertheless, they are generally accurate in relative terms (see Tables V and VI). This is always true for the exponential model. For instance, $\overline{\mu}_{\mathrm{var}}$ attains the lowest values, for the both nominal and estimated, for 1% hematocrit, whereas it becomes highest at 10% hematocrit (see column 11 of Tables V and VI). It may be noted that small errors in the size estimate translate into large errors in the optical absorption coefficient variance assessment [5]. This may be the reason why estimated $\overline{\mu}_{\mathrm{var}}$ differs from the actual one. For mixtures of RBCs and MCs, predicted and actual values show excel-

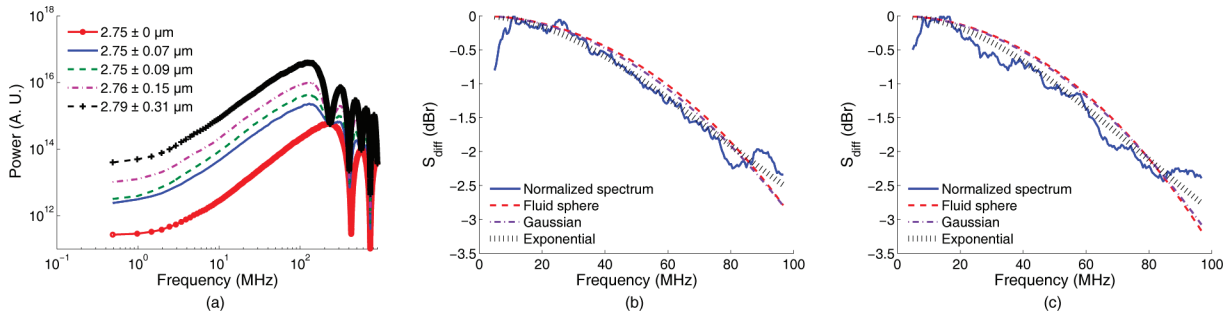

Fig. 10. (a) PA spectral lines for different mixtures of RBCs and MCs. (b)-(c) Plots of difference spectrum for 2.75 ± 0.09 and 2.79 ± 0.31, respectively. Fitted lines for the three correlation functions are also displayed (broken lines). The first sample behaved as the reference medium (i.e., the monodisperse sample).

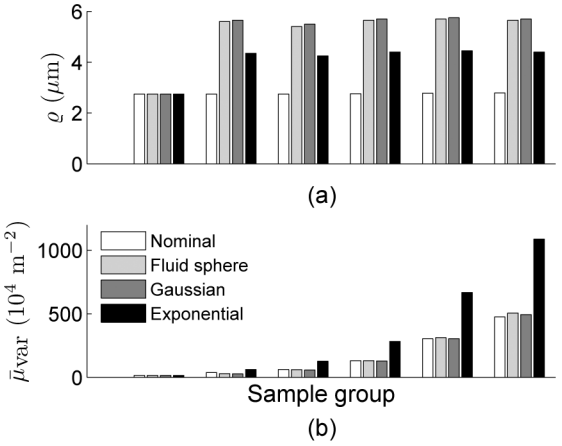

Fig. 11. (a) Numerical values of estimated radii of PA sources for diluted blood samples containing mixtures of RBCs and MCs. The true values are also provided for comparison. (b) Same as (a) but for the variance in the optical absorption coefficients.

lent agreement for the first two models [Table VII and Fig. 11(a)].

The performances of the models presented in this work have been tested on diluted samples as it is known from ultrasonic literature that such an approach works faithfully for sparse media. For such media, the boundary buildup is not strong (Fig. 3) and also PA power from individual sources add up independently. It turns out to be that the entire signal length may be used for the frequency domain analysis. However, for dense media, boundary buildup is very strong (as it appears from the literature [26], [27], [29]), and therefore, the spectral analysis should be conducted using central segment of RF line (Fig. 3). In the future, it would be of interest to investigate the validity of these models for characterizing dense media (e.g., blood). It may further be noted that in ultrasonic tissue characterization the variance in the acoustic impedance mismatch (γ) is decomposed as $|\langle\gamma^2\rangle - \langle\gamma\rangle^2| = \overline{n}V_{\rm s}\gamma_0^2$, where $\overline{n}$, $V_{\rm s}$, and γ_0^2 are the number of scatterers per unit volume, average volume of scatterers, and mean square acoustic impedance mismatch per particle, respectively. Such a factorization is possible because γ is assumed to be a zero mean random variable (i.e., $\langle\gamma\rangle = 0$) [5], [29]. With this simplification, it may be possible to determine $\overline{n}$ and γ_0^2 for a tissue medium. However, the average variance in the optical absorption coefficients cannot be decomposed in a similar fashion because $\langle\mu\rangle \neq 0$, and in fact, it is a random variable with a positive mean [29].

It may be emphasized that the spectral analysis for diluted blood samples has been performed in this study over a large bandwidth (5–100 MHz). As stated earlier, similar frequency range was utilized by Han *et al.* for characterizing cell pellet biophantoms and tumors *ex vivo* [44]. However, high-frequency acoustic waves cannot propagate much in tissue due to strong attenuation originating from scattering of waves by medium inhomogeneities. For example, the penetration depth in tissue is about 3 mm for a 50-MHz wave [16] so that it may not be feasible to detect high-frequency waves in practice associated with *in vivo* procedures. The present method will be most useful if it can provide quantitative information on tissue microstructure at low frequency range, where medical transducers work (<15 MHz) and also absorbers are not resolvable. Therefore, further investigations are required to examine the sensitivity of the models utilizing low bandwidth signals affected by scattering of light and acoustic waves and corrupted by electronic noise.

In this study, the calibration spectrum has been obtained from a medium that is similar to the test material. The same approach was also adopted by other groups [16], [46]. Nevertheless, Kumon *et al.* normalized their PA data by a spectrum generated from a hair fiber with a diameter of 30 μm [13]. PA signal emitted by a 200-nm gold film was considered as a reference signal by Hysi *et al.* [42]. Further efforts should be directed to select a suitable protocol for obtaining reference spectrum facilitating accurate estimates.

TABLE VII. A Comparison Between the Actual and the Extracted Values of the Mean Cell Size and the Variance in the Optical Absorption Coefficients for Samples Composed of Mixtures of RBCs and MCs Occupying a Volume Fraction of 5% for All Samples.

Nominal			Fluid sphere			Gaussian			Exponential		
ϱ (μm)	$\bar{\mu}_{\rm var}$ (10^4 m^{-2})	Frequency band (MHz)	ϱ (μm)	$\bar{\mu}_{\rm var}$ (10^4 m^{-2})	Err	ϱ (μm)	$\bar{\mu}_{\rm var}$ (10^4 m^{-2})	Err	ϱ (μm)	$\bar{\mu}_{\rm var}$ (10^4 m^{-2})	Err
2.75 ± 0 (22958, 0)	14.91	4.9–96.7	2.75	15.00	0	2.75	15.00	0	2.75	15.00	0
2.75 ± 0.07 (22838, 20)	38.02	4.9–96.7	5.60	28.75	2.6	5.65	28.00	2.4	4.35	62.00	1.4
2.75 ± 0.09 (22718, 40)	61.13	4.9–96.7	5.40	60.50	2.1	5.50	57.75	1.9	4.25	126.50	1.4
2.76 ± 0.15 (22357, 100)	130.37	4.9–96.7	5.65	131.50	1.5	5.70	128.25	1.3	4.40	282.50	0.7
2.78 ± 0.24 (21456, 250)	303.04	4.9–96.7	5.70	312.25	1.4	5.75	304.50	1.3	4.45	667.75	0.9
2.79 ± 0.31 (20554, 400)	475.11	4.9–96.7	5.65	506.00	1.5	5.70	493.50	1.4	4.40	1087.75	1.0

The numbers of RBCs and MCs in each sample are provided within the parentheses (first column). Err = $\Sigma_i|(o_i - e_i)|/|e_i|$ is related to the quality of a fitting (o_i and e_i denote observed and expected values, respectively).

In conclusion, a method to quantify parameters of optically inhomogeneous media is discussed. The corresponding inverse problem framework is deduced in detail. An analogous framework is extensively used in quantitative ultrasound. It is demonstrated that the mean size of solid beads can be estimated with good accuracy (error <10%) using the fluid sphere and Gaussian correlation models if the particle radius lies in the range ≥20 μm. The average size of fluid spheres approximating RBCs can be assessed by the exponential model with an accuracy of 22%. These results suggest that the method presented in this paper may have the ability to measure dimensions of tissue microstructures having size of tens of microns. The estimates for average variance in the optical absorption coefficients of particles exhibit good correlation with the nominal values. These two parameters together may have the ability to classify tissue types, and therefore, the technique discussed here may help to design a new tissue characterization strategy.

Acknowledgments

Stimulating discussions with Dr. S. Karmakar and Dr. M. Roy are gratefully acknowledged. The author also thanks the anonymous reviewers for their comments and suggestions. Based on these, several changes have been incorporated in the manuscript.

References

[1] K. K. Shung and G. A. Thieme, *Ultrasound Scattering in Biological Tissues*. Boca Raton, FL, USA: CRC Press, 1993.
[2] J. Mamou and M. L. Oelze, *Quantitative Ultrasound in Soft Tissues*. New York, NY, USA: Springer, 2013.
[3] F. L. Lizzi, M. Greenebaum, E. J. Feleppa, M. Elbaum, and D. J. Coleman, "Theoretical framework for spectrum analysis in ultrasonic tissue characterization," *J. Acoust. Soc. Am.*, vol. 73, no. 4, pp. 1366–1373, 1983.
[4] F. L. Lizzi, M. Ostromogilsky, E. J. Feleppa, M. C. Rorke, and M. M. Yaremko, "Relationship to ultrasonic spectral parameters to features of tissue microstructure," *IEEE Trans. Ultrason. Ferroelectr. Freq. Control*, vol. 34, no. 3, pp. 319–329, 1987.
[5] M. F. Insana, R. F. Wagner, D. G. Brown, and T. J. Hall, "Describing small-scale structure in random media using pulse-echo ultrasound," *J. Acoust. Soc. Am.*, vol. 87, no. 1, pp. 179–192, 1990.
[6] E. J. Feleppa, F. L. Lizzi, D. J. Coleman, and M. M. Yaremko, "Diagnostic spectrum analysis in ophthalmology: A physical perspective," *Ultrasound Med. Biol.*, vol. 12, no. 8, 623–631, 1986.
[7] E. J. Feleppa, T. Liu, A. Kalisz, M. C. Shao, N. Fleshner, and V. Reuter, "Ultrasonic spectral-parameter imaging of the prostate," *Int. J. Imaging Syst. Technol.*, vol. 8, no. 1, pp. 11–25, 1997.
[8] M. F. Insana and T. J. Hall, "Characterizing the microstructure of random media using ultrasound," *Phys. Med. Biol.*, vol. 35, no. 10, pp. 1373–1386, 1990.
[9] F. T. Yu and G. Cloutier, "Experimental ultrasound characterization of red blood cell aggregation using the structure factor size estimator," *J. Acoust. Soc. Am.*, vol. 122, no. 1, pp. 645–656, 2007.
[10] R. M. Vlad, S. Brand, A. Giles, M. C. Kolios, and G. J. Czarnota, "Quantitative ultrasound characterization of responses to radiotherapy in cancer mouse models," *Clin. Cancer Res.*, vol. 15, no. 6, pp. 2067–2075, 2009.
[11] M. L. Oelze, W. D. O'Brien Jr., J. P. Blue, and J. F. Zachary, "Differentiation and characterization of rat mammary fibroadenomas and 4T1 mouse carcinomas using quantitative ultrasound imaging," *IEEE Trans. Med. Imaging*, vol. 23, no. 6, pp. 764–771, 2004.
[12] J. Mamou, A. Coron, M. L. Oelze, E. Saegusa-Beecroft, M. Hata, P. Lee, J. Machi, E. Yanagihara, P. Laugier, and F. J. Feleppa, "Three-dimensional high-frequency backscatter and envelope quantification of cancerous human lymph nodes," *Ultrasound Med. Biol.*, vol. 37, no. 3, pp. 345–357, 2011.
[13] R. E. Kumon, C. X. Deng, and X. Wang, "Frequency-domain analysis of photoacoustic imaging data from prostate adenocarcinoma tumors in a murine model," *Ultrasound Med. Biol.*, vol. 37, no. 5, pp. 834–839, 2011.
[14] Y. Yang, S. Wang, C. Tao, X. Wang, and X. Liu, "Photoacoustic tomography of tissue subwavelength microstructure with a narrowband and low frequency system," *Appl. Phys. Lett.*, vol. 101, no. 3, art. no. 034105, 2012.
[15] G. Xu, I. A. Dar, C. Tao, X. Liu, C. X. Deng, and X. Wang, "Photoacoustic spectrum analysis for microstructure characterization in biological tissue: A feasibility study," *Appl. Phys. Lett.*, vol. 101, no. 22, art. no. 221102, 2012.
[16] S. Wang, C. Tao, X. Wang, and X. Liu, "Quantitative detection of stochastic microstructure in turbid media by photoacoustic spectral matching," *Appl. Phys. Lett.*, vol. 102, no. 11, art. no. 114102, 2013.
[17] L. V. Wang and S. Hu, "Photoacoustic tomography: In vivo imaging from organelles to organs," *Science*, vol. 335, no. 6075, pp. 1458–1462, 2012.
[18] H. F. Zhang, K. Maslov, G. Stoica, and L. V. Wang, "Functional photoacoustic microscopy for high-resolution and noninvasive *in vivo* imaging," *Nat. Biotechnol.*, vol. 24, no. 7, pp. 848–851, 2006.
[19] P. Beard, "Biomedical photoacoustic imaging," *Interface Focus*, vol. 1, no. 4, pp. 602–631, 2011.
[20] R. K. Saha and M. C. Kolios, "A simulation study on photoacoustic signals from red blood cells," *J. Acoust. Soc. Am.*, vol. 129, no. 5, pp. 2935–2943, 2011.
[21] G. J. Diebold, "Photoacoustic monopole radiation: Waves from objects with symmetry in one, two and three dimensions," in *Photoacoustic Imaging and Spectroscopy*. L. V. Wang, Ed. London, UK: Taylor and Francis Group, LLC, 2009, ch. 1, pp. 3–17.
[22] A. Ishimaru, *Wave Propagation and Scattering in Random Media*. New York, NY, USA: Academic Press, 1978, ch. 4, pp. 69–92.
[23] R. K. Saha and M. C. Kolios, "Effects of erythrocyte oxygenation on optoacoustic signals," *J. Biomedical Optics*, vol. 16, no. 11, art. no. 115003, 2011.
[24] E. Hysi, R. K. Saha, and M. C. Kolios, "On the use of photoacoustics to detect red blood cell aggregation," *Biomed. Opt. Express*, vol. 3, no. 9, pp. 2326–2338, 2012.
[25] E. Hysi, R. K. Saha, and M. C. Kolios, "Photoacoustic ultrasound spectroscopy for red blood cell aggregation and oxygenation," *J. Biomedical Optics*, vol. 17, no. 12, art. no. 125006, 2012.
[26] R. K. Saha, S. Karmakar, and M. Roy, "Computational investigation on the photoacoustics of malaria infected red blood cells," *PLoS ONE*, vol. 7, no. 12, art. no. e51774, 2012.
[27] R. K. Saha, M. Roy, and A. Datta, "Simulation study on the photoacoustics of cells with endocytosed gold nanoparticles," *Curr. Sci.*, vol. 106, no. 11, pp. 1554–1559, 2014.
[28] R. K. Saha, "Computational modeling of photoacoustic signals from mixtures of melanoma and red blood cells," *J. Acoust. Soc. Am.*, vol. 136, no. 4, pp. 2039–2049, 2014.
[29] Z. Guo, L. Li, and L. V. Wang, "On the speckle-free nature of photoacoustic tomography," *Med. Phys.*, vol. 36, no. 9, pp. 4084–4088, 2009.
[30] L. Chernov, *Wave Propagation in a Random Medium*. New York, NY, USA: McGraw-Hill, 1960.
[31] J. C. Bamber, "Theoretical modelling of the acoustic scattering structure of human liver," *Acoust. Lett.*, vol. 3, no. 6, pp. 114–119, 1979.
[32] D. K. Nassiri and C. R. Hill, "The use of angular acoustic scattering measurements to estimate structural parameters of human and animal tissues," *J. Acoust. Soc. Am.*, vol. 79, no. 6, pp. 2048–2054, 1986.
[33] R. N. Bracewell, *The Fourier Transform and Its Applications*, 2nd ed. New York, NY, USA: McGraw-Hill, 1978.
[34] E. L. Hinrichsen, J. Feder, and T. Jøssang, "Random packing of disks in two dimensions," *Phys. Rev. A*, vol. 41, no. 8, art. no. 4199–4209, 1990.
[35] T. Aste, "Circle, sphere, and drop packing," *Phys. Rev. E*, vol. 53, no. 3, pp. 2571–2579, 1996.

[36] X. Wang, C. Xie, G. Ku, L. V. Wang, and G. Stoica, "Noninvasive imaging of hemoglobin concentration and oxygenation in the rat brain using high-resolution photoacoustic tomography," *J. Biomedical Optics*, vol. 11, no. 2, art. no. 024015, 2006.
[37] R. O. Esenaliev, I. V. Larina, K. V. Larin, D. J. Deyo, M. Motamedi, and D. S. Prough, "Optoacoustic technique for noninvasive monitoring of blood oxygenation: A feasibility study," *Appl. Opt.*, vol. 41, no. 22, pp. 4722–4731, 2002.
[38] R. M. Weight, J. A. Viator, P. S. Dale, C. W. Caldwell, and A. E. Lisle, "Photoacoustic detection of metastatic melanoma cells in the human circulatory system," *Opt. Lett.*, vol. 31, no. 20, pp. 2998–3000, 2006.
[39] E. Galanzha, E. V. Shashkov, P. M. Spring, J. Y. Suen, and V. P. Zharov, "In vivo, noninvasive, label-free detection and eradication of circulating metastatic melanoma cells using two-color photoacoustic flow cytometry with a diode laser," *Cancer Res.*, vol. 69, no. 20, pp. 7926–7934, 2009.
[40] R. P. Solano, F. I. Ramirez-Perez, J. A. Castorena-Gonzalez, E. A. Anell, G. Gutiérrez-Juárez, and L. Polo-Parada, "An experimental and theoretical approach to the study of the photoacoustic signal produced by cancer cells," *AIP Adv.*, vol. 2, art. no. 011102, 2012.
[41] M. I. Khan and G. J. Diebold, "The photoacoustic effect generated by an isotropic solid sphere," *Ultrasonics*, vol. 33, no. 4, pp. 265–269, 1995.
[42] E. Hysi, D. Dopsa, and M. C. Kolios, "Photoacoustic tissue characterization using envelope statistics and ultrasonic spectral parameters," *Proc. SPIE*, vol. 8943, art. no. 89432E, 2014.
[43] K. A. Topp, J. F. Zachary, and W. D. O'Brien Jr., "Quantifying B-mode images of in vivo rat mammary tumors by the frequency dependence backscatter," *J. Ultrasound Med.*, vol. 20, pp. 605–612, 2001.
[44] A. Han, R. Abuhabsah, R. J. Miller, S. Sarwate, and W. D. O'Brien Jr., "The measurement of ultrasound backscattering from cell pellet biophantoms and tumors *ex vivo*," *J. Acoust. Soc. Am.*, vol. 134, no. 1, pp. 686–693, 2013.
[45] T. A. Tuthill, R. H. Sperry, and K. J. Parker, "Deviations from Rayleigh statistics in ultrasonic speckle," *Ultrasonic Imaging*, vol. 10, pp. 81–89, 1988.
[46] P. V. Chitnis, J. Mamou, A. Sampthkumar, and E. J. Feleppa, "Spectrum analysis of photoacoustic signals for tissue classification," *Proc. SPIE*, vol. 8943, art. no. 89432J, 2014.

Ratan K. Saha obtained his B.Sc. degree in physics from the University of North Bengal, Siliguri, India, in 1996 and M.Sc. degree in physics from Jadavpur University, Kolkata, India, in 1999. He carried out his Ph.D. work at the Saha Institute of Nuclear Physics, Kolkata, from 2000 to 2006. He worked as a postdoctoral fellow in the Laboratory of Biorheology and Medical Ultrasonics, Research Center of the University of Montreal Hospital, Montreal, Canada, from 2007 to 2008; in the Department of Physics, Ryerson University, Toronto, Canada, from 2009 to 2011; and in the Saha Institute of Nuclear Physics from 2011 to 2013. Since October 2013, he has been a CSIR Pool Officer at the Saha Institute of Nuclear Physics. His current research interests include characterization and imaging of soft tissues using ultrasonics and photoacoustics.